Cell Reports
Physical Science

CellPress
OPEN ACCESS

Article

Transforming 3D-printed mesostructures into multimodal sensors with nanoscale conductive metal oxides

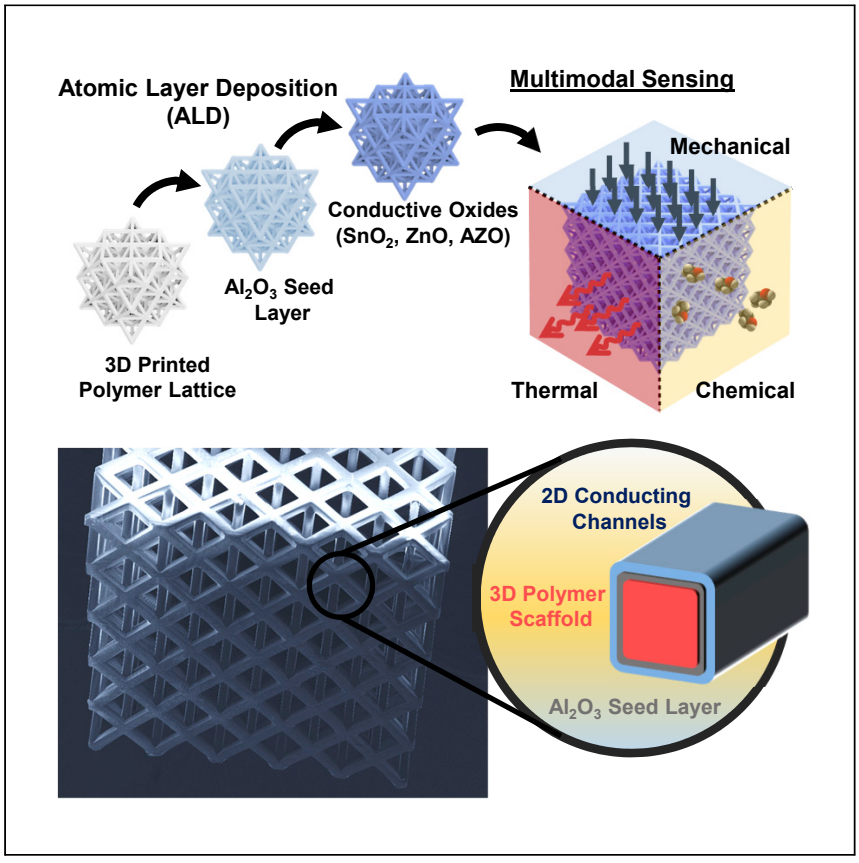

Huddy et al. present a strategy for transforming additively manufactured mesostructures into 3D electronics by growing nanoscale conducting oxides on 3D-printed polymers. The authors apply graph theory to design mesostructures for sensing chemical and thermophysical stimuli, geometrically boosting sensitivity 100× over conventional films to enable a new class of 3D-printable sensors.

Julia E. Huddy, Md Saifur Rahman, Andrew B. Hamlin, Youxiong Ye, William J. Scheideler

william.j.scheideler@dartmouth.edu

Highlights

Microstereolithography is integrated with low-temperature atomic layer deposition

Conducting oxides (ZnO, AZO, SnO_2) functionalize 3D mesostructured lattices

Nanometer thickness control determines oxide coating electrostatics

The 3D geometries enhance sensor response to chemical, thermal, and mechanical stimuli

Huddy et al., Cell Reports Physical Science 3, 100786
March 16, 2022
https://doi.org/10.1016/j.xcrp.2022.100786

Cell Reports
Physical Science

CellPress
OPEN ACCESS

Article

Transforming 3D-printed mesostructures into multimodal sensors with nanoscale conductive metal oxides

Julia E. Huddy,[1] Md Saifur Rahman,[1] Andrew B. Hamlin,[1] Youxiong Ye,[1] and William J. Scheideler[1,2,*]

SUMMARY

Additively manufactured (AM) three-dimensional (3D) mesostructures exhibit geometrically optimal mechanical, thermal, and optical properties that could drive future microrobotics, energy harvesting, and biosensing technologies at the micrometer to millimeter scale. We present a strategy for transforming AM mesostructures into 3D electronics by growing nanoscale conducting films on 3D-printed polymers. This highly generalizable method utilizes precision atomic layer deposition (ALD) of conducting metal oxides on ultrasmooth photopolymer lattices printed by high-resolution microstereolithography. We demonstrate control of 3D electronic transport by tuning conformal growth of ultrathin amorphous and crystalline conducting metal oxides. To understand the scaling of 3D electrical properties, we apply graph theory to compute network resistance and precisely design the 3D mesostructures' conductivity. Finally, we demonstrate 3D-enhanced multimodal sensing of chemical, thermal, and mechanical stimuli, geometrically boosting sensitivity by 100× over 2D films and enabling a new class of low-power, 3D-printable sensors.

INTRODUCTION

Engineered 3D lattices at the mesoscale (10 μm to 1 mm) exhibit optimal geometries for new applications such as lightweight mechanical metamaterials with extreme stiffness[1,2] or bioprinted tissue scaffolds[3] requiring control of pore size for regenerative tissue growth.[4] The periodic, porous internal structure provides opportunities for tuning the multifunctional response of 3D lattices to various mechanical and thermal stimuli,[5] as well as electric[6] and magnetic fields.[7] Multimaterial 3D lattices can begin to leverage this geometric tunability to enhance device performance in electrochemical energy storage[8] or shape-shifting heterogeneous structures.[9] Importantly, 3D lattices offer the ability to engineer properties that cannot be achieved with random porous materials such as foams, for example, to engineer channels for efficient mass transport in redox flow batteries.[10]

Currently, 3D mesoscale lattices require additive manufacturing methods such as stereolithography (SLA)[11] and two-photon nanolithography,[12] because micromachining methods are inherently limited in their ability to fabricate complex 3D geometries. This traditional limitation of microfabrication also means that conventional electronic microsystems (printed circuit boards [PCBs], integrated circuits [ICs], etc.) remain stacks of planar structures due to the segmented and serial nature of the deposition, pattern, and etch paradigm. Future advances in additive manufacturing could overcome this barrier to miniaturized, multifunctional systems

[1]Thayer School of Engineering, Dartmouth College, Hanover, NH 03755, USA

[2]Lead contact

*Correspondence: william.j.scheideler@dartmouth.edu

https://doi.org/10.1016/j.xcrp.2022.100786

Please cite this article in press as: Huddy et al., Transforming 3D-printed mesostructures into multimodal sensors with nanoscale conductive metal oxides, Cell Reports Physical Science (2022), https://doi.org/10.1016/j.xcrp.2022.100786

if electronic functionality can be integrated in 3D mesostructures while leveraging their geometric advantages.

Recent work has begun the integration of electrically functional materials with 3D printing. For example, high-resolution 3D printing by SLA has been expanded from photopolymers to include percolative conductive polymer nanocomposites[13] and polymer-derived ceramic materials.[14] In addition, electroless and electroplating post processes have been developed for depositing micrometer-thick metal layers on 3D lattices for applications in catalysis[15] and energy storage.[8,16,17] Alternatively, extrusion-based 3D printing methods are now available to fabricate 3D lattices comprising bulk metals,[18] but these methods have lower printing resolution than SLA and two-photon lithography[11] and require sintering at elevated temperatures.[19] However, these methods for bulk material fabrication are unable to integrate nanoscale films of semiconducting and conducting materials with 3D mesostructures. Nanoscale thin films are a promising class of materials specifically for 3D-printed device applications because, unlike bulk structures, they can be exploited for their surface-driven electrostatic sensitivity to chemisorption and physisorption in various chemical[20] and biological sensing applications.[21]

In this work, we present a strategy for transforming 3D-printed polymers into versatile electronic sensors using conductive lattices fabricated by microstereolithography (μSLA) and functionalized through conformal atomic layer deposition (ALD). μSLA offers high-resolution, large-area printing based on a step-and-repeat modality, which we exploit to control the conductivity of 3D-printed lattices through structural scaling from the millimeter to the microscale. At the nanoscale, ALD allows unprecedented engineering of 3D electronic transport by growing ultrathin amorphous and crystalline metal oxides (Al_2O_3, ZnO, SnO_2) at temperatures below the glass-transition temperature (T_g) of the photopolymer lattice. Here, for the first time, we demonstrate that atomic layer control of metal oxide thickness modulates the electrostatic properties of 3D lattices, enhancing their response to thermal, mechanical, fluidic, and chemical stimuli.

These electrically conductive lattices illustrate a fundamental advantage of 3D mesostructures versus traditional 2D films for surface-driven physicochemical sensing that cannot be achieved with bulk materials. We expect this approach will broaden the scope of additive manufacturing beyond structural components. Importantly, the low-temperature processing methods developed can deliver these advantages through direct integration with silicon microelectronics, unlocking a pathway to a new class of additively manufactured wireless sensors that can leverage the properties of nanoscale materials for enhancing low-power sensing.

RESULTS AND DISCUSSION

μSLA generation of high-resolution 3D structures

In this work, we use μSLA to generate high-resolution 3D structures in a variety of lattice geometries. The μSLA system exposes a photopolymer resin with top-down illumination through projection optics using a 405 nm ultraviolet light-emitting diode. Careful design of the optics allows this process to scale down to 2 μm pixels. Figure 1 shows scanning electron microscope (SEM) images of this wide range of 3D structures coated with conductive ZnO and SnO_2 films. These structures span length scales from 10 μm features to millimeter-scale features, including free-standing plates, octet, cubic, and tetrakaidecahedron lattices (Figure S1) and spherical volumes filled with octet lattice. This shows the power of μSLA (Figure 1I) to form

Please cite this article in press as: Huddy et al., Transforming 3D-printed mesostructures into multimodal sensors with nanoscale conductive metal oxides, Cell Reports Physical Science (2022), https://doi.org/10.1016/j.xcrp.2022.100786

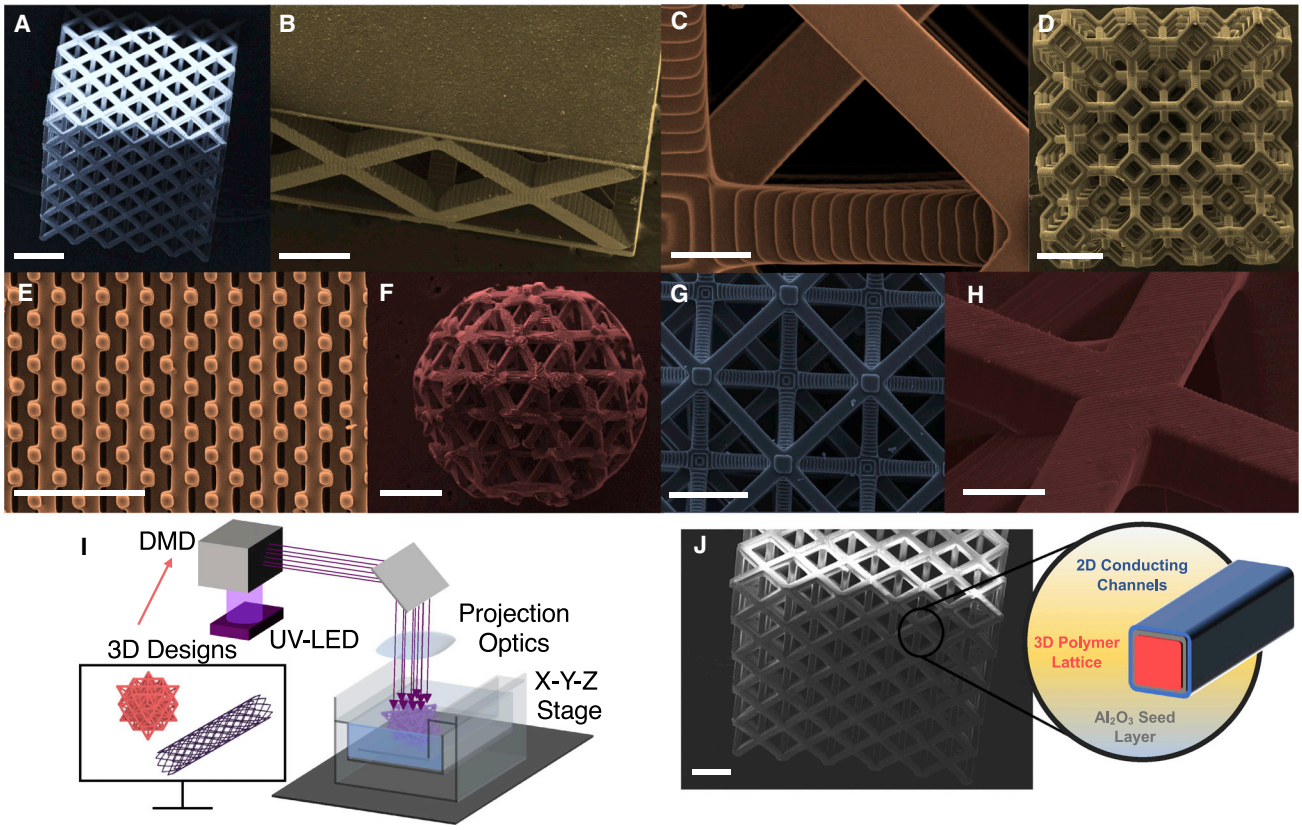

Figure 1. Three-dimensional conductive mesostructures printed by microstereolithography

(A–H) Various metal-oxide-coated mesostructures spanning length scales from 10 μm features to 1 mm features in cubic volumes of octet lattices (A–C, G, and H), wood pile lattices (E), tetrakaidecahedron lattices (D), and spherical volumes of octet lattice (F).

(I) Scheme for microstereolithography printing.

(J) Layer cross section showing 2D conducting channels coated onto 3D polymer lattice using a conformal seed layer. Scale bars, 500 μm (A, B, D, F, and J), 20 μm (C), and 100 μm (E, G, and H).

high-resolution mesostructures that can achieve varying porosities from 50% to above 90% volume porosity without suffering from the mechanical fragility that limits bulk porous materials such as aerogels. Three-dimensional structures such as the octet lattice provide the mechanical stability optimal for resisting mechanical stresses during 3D printing by μSLA. The octet lattice topologies used here have high shear moduli and high surface area-to-volume ratios due to their internal support structure.[22,23] The mechanics of these lattices is essential because 3D printing of high-resolution lattices demands struts with sufficient mechanical strength to resist viscous forces applied by the resin leveling during printing.

Interestingly, these structures produced by industrial 3D fabrication have an ultrasmooth surface finish sufficient to facilitate uniform 3D conformal coating (Figure 1J) of electronic films. Stylus profilometry (Figure S2) reveals that the interfaces parallel to layer formation exhibit a low root-mean-square (RMS) roughness of below 31 nm, while surfaces perpendicular to the build plane inherit the sinusoidal waviness induced by the layer-by-layer SLA process, resulting in an RMS roughness of approximately 140 nm. In comparison, other 3D printing methods, such as fused deposition modeling (FDM) and binder jet printing, produce structures with a surface roughness of 2–200 μm,[24,25] making it harder to deposit ultrathin films onto the materials. Figure 1C illustrates a magnified view of the smooth surfaces of faces parallel to the

Please cite this article in press as: Huddy et al., Transforming 3D-printed mesostructures into multimodal sensors with nanoscale conductive metal oxides, Cell Reports Physical Science (2022), https://doi.org/10.1016/j.xcrp.2022.100786

build plane of the μSLA process, while Figure 1H shows micrometer-scale ridges produced on the lateral faces of parts. This phenomenon is typical for SLA, but could eventually be alleviated by advanced gray-scale lithography methods.[11]

Atomic layer deposition of nanoscale 3D conductors

Given the ultrasmooth surface of these μSLA parts, we are able to use ALD, a high-precision method for growth of nanoscale thin films, to deposit functional metal oxide materials at low temperatures onto the 3D structures. ALD allows highly uniform, *conformal* growth of various dielectrics, semiconductors, and conductors useful in microelectronics as well as a variety of other applications in energy and sensing. In this work, we utilize ALD to coat microscale 3D-printed polymer lattices with conducting (SnO_2, ZnO:Al) and semiconducting (ZnO) metal oxide films. This strategy could be extensible to a broad range of functional metal oxide thin films as well as a range of 3D-printed polymer lattices.

ALD growth can be inhibited by polymers such as polymethylmethacrylate (PMMA) and poly(vinyl pyrrolidone) (PVP),[26] depending on growth conditions and precursor chemistry. The ALD process is also known to induce subsurface growth in some polymer substrates (polyethylene),[27] which can effectively inhibit the formation of functional electronic thin films.[27] This phenomenon has also been studied in the context of vapor phase infiltration of ALD precursors such as trimethylaluminum (TMA) into polymers for fabricating hybrid organic/inorganic structures.[28] Mechanistic studies of ALD growth on polymers have differentiated lower growth-temperature regimes in which overcoats are formed and higher-temperature regimes in which subsurface diffusion leads to particle growth and roughening.[29]

In this work, we developed a low-temperature-deposited (100°C) seed layer of Al_2O_3, which then leads to the ability to uniformly coat transparent conductive films composed of ZnO, ZnO:Al (AZO), and SnO_2 on 3D structures fabricated by μSLA. Without an Al_2O_3 seed layer, growth of the conductive films on the 3D-printed polymers is inhibited. We also noticed that there is a zone of inhibited growth surrounding the part in the ALD chamber (Figure S3), which can be eliminated via deposition of the seed layer. The ALD growth process on 3D-printed polymers depends critically on growth temperature. We observed that the low temperature (~100°C) ALD process forms a 10–20 nm seed layer passivating the 3D surface and leading to a high-precision "ALD" coating regime (Figure 2A) for subsequent deposition of distinct functional conductive and semiconducting layers, as shown in the cross-sectional SEM images and energy-dispersive spectroscopy (EDS) maps in Figure 2B. With this low-temperature seed layer, the growth of continuous conductive films was achieved across a wide range of temperatures up to and slightly above the T_g of the acrylate polymer lattices used in this work (172°C). In addition, we demonstrated that this seed layer enabled the growth of conductive films on 3D parts printed from various commercial SLA polymer resins, indicating that this process is applicable to a range of acrylate and epoxy photopolymers.

Material characterization of 3D conductive coatings

X-ray diffraction (XRD) studies of the coated 3D structures (Figure 2C) show the amorphous phase for the Al_2O_3 seed layers and the SnO_2 conductor films, as previously reported for low-temperature thermal ALD growth of these materials.[30] The 3D ZnO films, however, show (100), (002), and (101) peaks consistent with the nanocrystalline hexagonal wurtzite phase[31] that match the peak locations for identical ZnO growths on planar substrates of SiO_2 (Figure S4). The X-ray photoelectron spectroscopy (XPS) studies shown in Figures 2D–2F illustrate the chemical composition of

Please cite this article in press as: Huddy et al., Transforming 3D-printed mesostructures into multimodal sensors with nanoscale conductive metal oxides, Cell Reports Physical Science (2022), https://doi.org/10.1016/j.xcrp.2022.100786

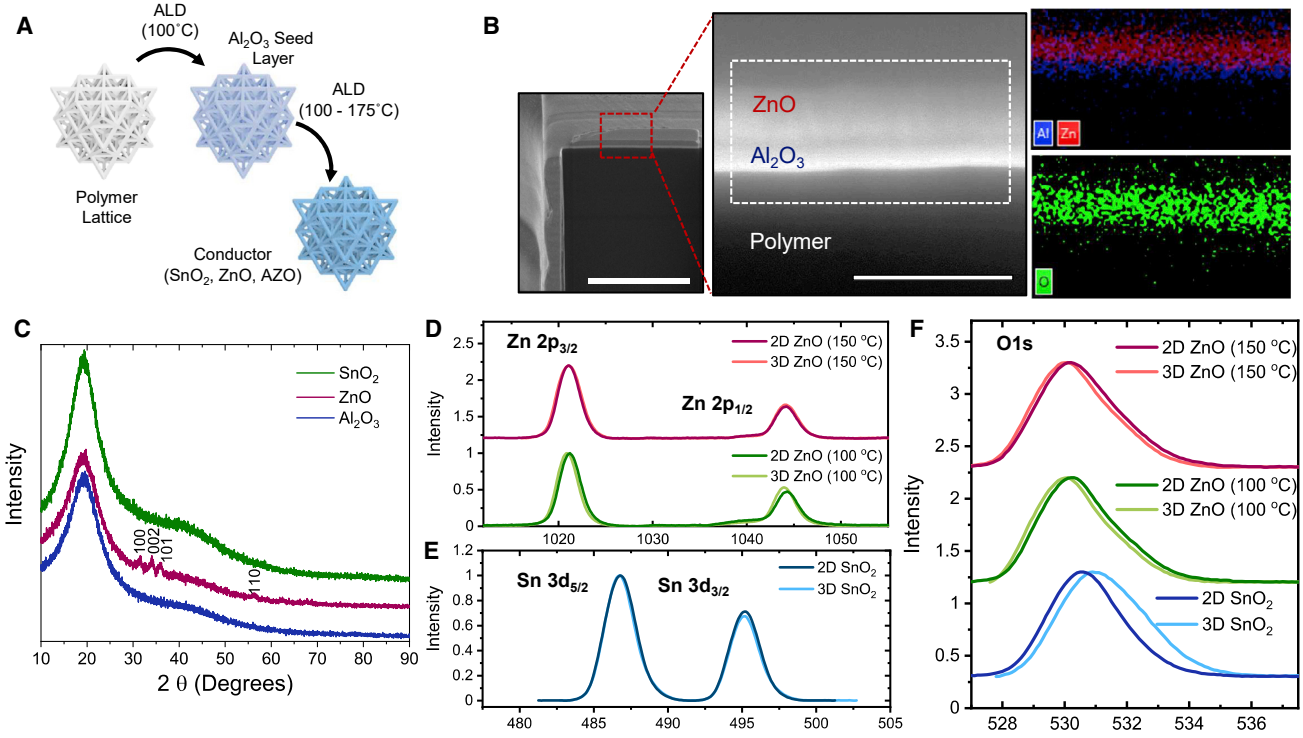

Figure 2. Demonstration of metal oxide growth on 3D-printed mesostructures

(A) Scheme for conformal coating of 3D-printed mesostructures using a low-temperature (100°C) Al_2O_3 seed layer and subsequent ALD growth of conducting and semiconducting films of SnO_2, ZnO, and AZO.

(B) Cross section high-resolution SEM imaging of conformal ALD ZnO films on Al_2O_3 seed layers coated onto the polymer lattices. EDS images (right) illustrate distinct Al_2O_3 seed layer and ZnO coating. Scale bars, 10 μm (left) and 500 nm (center).

(C) XRD spectra for metal oxide films (ZnO, Al_2O_3, SnO_2) coated onto 3D polymer lattices.

(D and E) XPS scans of (D) Zn 2p peaks and (E) Sn 3d peaks for 2D and 3D films.

(F) XPS scans of O 1s peaks for 2D and 3D films of SnO_2 and ZnO deposited at 100°C and 150°C.

ALD-grown ZnO and SnO_2 films deposited on the 3D polymer lattices in comparison with 2D films deposited on SiO_2 wafers. The metal peaks for Zn (2p) and Sn (3d) exhibit strong correspondence between the 2D and the 3D samples. This is true across the range of growth temperatures, as shown for ZnO deposited at 100°C and 150°C. The comparison of the O (1s) peaks shown in Figure 2F indicates the ability for 3D ALD growth to produce films with similar stoichiometry (ZnO, SnO_2) on polymer lattices compared with traditional 2D growth. This is particularly important for achieving high conductivity in these functional metal oxide materials.

Electrical characterization of 3D conductive lattices

The 3D conductive lattices coated with ZnO, AZO, and SnO_2 were measured electrically by depositing conformal Au contacts on opposing faces by masked sputter deposition (Figure S5) and probing with a semiconductor microprobe station (Figure S6). Without deposition of the conducting oxide (ZnO, SnO_2, or AZO), the 3D lattices are non-conductive (Figure S7); however, after coating, the 3D lattices demonstrate high conductivity even for ultrathin films formed by only 40 cycles of ALD (~7 nm thickness). Figure 3A shows the I-V response of the lattices, illustrating the ohmic conduction across an AZO-coated 3D structure with various ALD growth cycle counts from 40 to 400. The effective resistance of the 3D structures scales strongly with the thickness, as expected. Figure 3B compares the resistance of AZO-coated 3D lattices with the measured 2D sheet resistance, showing the strong enhancement of conductance for

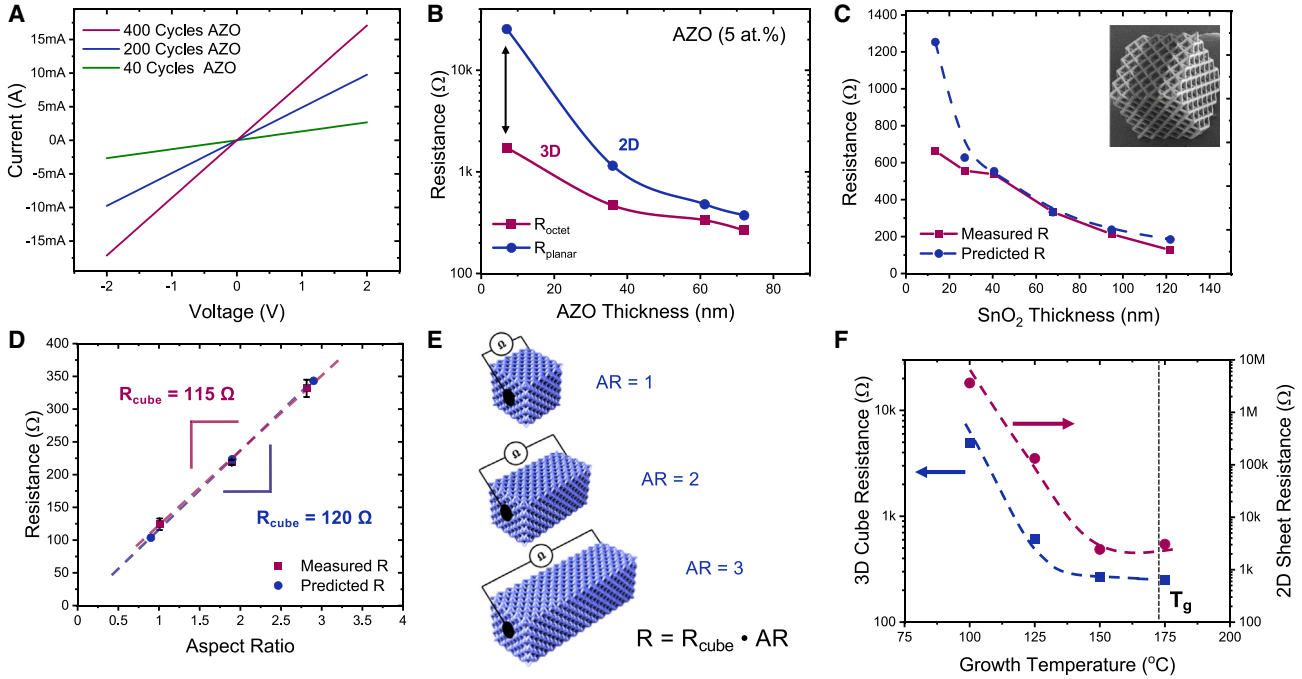

Figure 3. Electronic properties of ALD-coated 3D-printed octet lattices

(A) Ohmic conduction through AZO-coated conductive 3D lattices with varying ALD cycle counts.

(B) Resistance versus thickness for AZO films of various thicknesses in 2D and 3D geometries grown at 150°C.

(C) Resistance versus thickness for SnO_2 films of various thicknesses compared between the model (blue) and the measured data (purple). Inset shows octet cubic structure with Au sputtered contacts for electrical measurement.

(D) Resistance versus aspect ratio for AZO coated octet lattices compared between the model (blue) and the measured (purple) data.

(E) Schematic showing octet lattices with different aspect ratios (ARs) and how they were measured.

(F) Resistance versus growth temperature for 3D structures with 30 nm ZnO films (blue) and matching 2D ZnO films at each temperature (purple) with the polymer lattice T_g indicated in gray. Dashed lines are included as a guide to the eye.

3D networks, which can, essentially, fold nanoscale films into their internal geometries with higher total surface area, offering many parallel paths for current conduction. Similarly, the resistance of 3D lattices coated in SnO_2 can be reduced via deposition of thicker films, reaching the predicted resistances of below 200 Ω (Figure 3C). Our model also closely predicts the resistance of 3D lattices as the geometry is changed, as shown in Figure 3D, which shows the predicted and measured resistances of AZO-coated octet lattices with varied aspect ratio. Figure 3E emphasizes the size difference between the lattices and illustrates how they were contacted during measurement (Figure S8). Controlling the growth temperature allows deposition of more conductive 3D networks of ZnO, AZO, and SnO_2, as illustrated in Figure 3F, for films grown at temperatures between 100°C and 175°C. ZnO and SnO_2 films grown in this temperature range achieve resistivities of 8.5×10^{-3} and 4×10^{-2} Ω-cm, respectively, which are typical of these ALD-processed materials.[32,33] Interestingly, the ALD process produces highly conductive 3D networks from ultrathin films (30 nm ZnO), even when operating slightly above the T_g of the polymer lattice (T_g 172°C). The ability of our ALD method to deposit high-quality films in 3D geometries in this temperature range from 100°C to 175°C will facilitate the application of this method to a variety of new electronic material systems.

Modeling 3D conductance with graph theory

The 3D conductive lattices in this work are unique in their ability to control the porosity, surface area, and electrical conductivity in 3D with great precision. Unlike any existing porous composite material with stochastically varying properties, these

Please cite this article in press as: Huddy et al., Transforming 3D-printed mesostructures into multimodal sensors with nanoscale conductive metal oxides, Cell Reports Physical Science (2022), https://doi.org/10.1016/j.xcrp.2022.100786

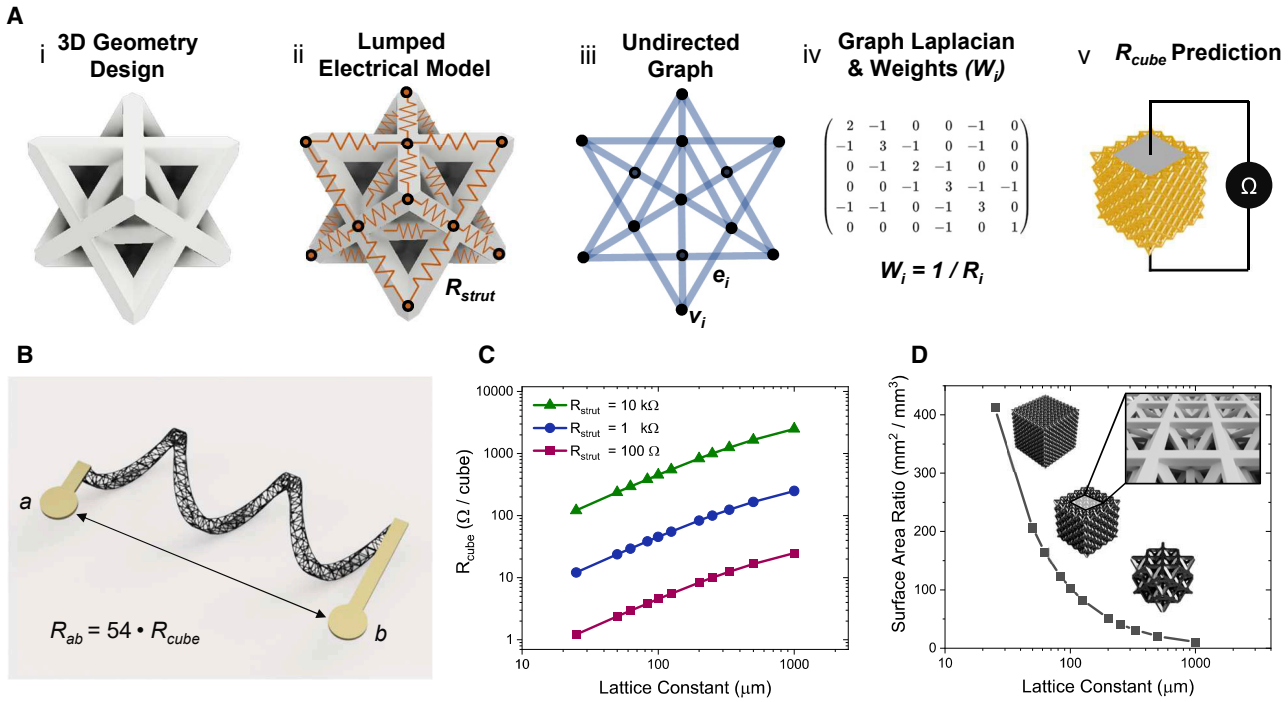

Figure 4. Graph theory model and predictions of 3D lattice conductance

(A) Scheme for modeling 3D conductive structures (i), by applying a lumped electrical model (ii), subsequently converted to an undirected graph (iii), for which the graph Laplacian is computed (iv), and used to predict R_{cube} (v).

(B) A 3D coiled lattice with gold pads for electrical measurement, indicating the predicted resistance of the overall structure based on the lattice type.

(C) Predicted conductivity for 3D octet lattice networks with varying lattice constant for three different strut resistances.

(D) The 3D surface area normalized by the 2D structural footprint for cubic volumes of octet lattices of varying lattice constant and 5:1 aspect ratio beams. Inset shows cubic volumes of octet lattice with varying lattice constant.

lattices can be architected in any conceivable 3D structure to achieve a specific conductance. We have developed an approach adapted from graph theory and network science[34] for computing the conductance of arbitrarily complex 3D networks. This approach utilizes a lumped element representation implemented as an undirected graph with edge weights corresponding to each strut's conductance ($G_i = 1/R_{strut}$), as shown in Figure 4A. The strut resistance (R_{strut}) is then calculated based on the geometry of the square profile beams (length L, width D) as well as the thickness (t) and resistivity (ρ) of the metal oxide coatings:

$$R_{\text{strut}} = \frac{L\rho}{4\,Dt}. \qquad \text{(Equation 1)}$$

Our method then consists of generating an adjacency matrix and computing a weighted, pseudo-inverse Laplacian, $Q^{\dagger}$, similar to recent work applied to efficiently analyze electrical networks represented as graphs.[34] We calculate the effective resistance between any two points in an arbitrary 3D structure using the matrix $Q^{\dagger}$, as follows:

$$R_{ab} = Q^{\dagger}(a,a) - 2\,Q^{\dagger}(a,b) + Q^{\dagger}(b,b). \qquad \text{(Equation 2)}$$

Building off recent theoretical work for efficiently computing 3D resistor meshes,[35] we apply the weighted Laplacian method to model a range of finite octet lattices filling a 1 mm^3 cubic volume with varied lattice constants (Figure S9). This allows us to compute a volumetric resistance quantity we label as R_{cube}, which can be compared against our experimental measurements of oxide-coated 3D-printed octet lattices. R_{cube} has dimensions Ω/cube, forming a 3D analog to a 2D sheet resistance (Ω/square) for 3D

microarchitected materials. The volumetric resistance of the lattice structures, R_{cube}, can be controlled purely by scaling the lattice constant or by adjusting the conductance of the individual struts (tunable via the ALD cycle count). To model complex 3D structures with lattice infill, such as the corkscrew structure shown in Figure 4B, we can scale the computed base unit resistance, R_{cube}, by multiplying by an appropriate 3D aspect ratio to determine the resistance from point *a* to point *b* (R_{ab}). Figure 4C displays the computed resistance per cubic volume, R_{cube}, for 3D octet structures with varying lattice constants from 25 to 1,000 μm. Finer 3D lattices naturally offer additional parallel paths for current conduction, providing a lower volumetric resistance, R_{cube}, for a given 1 mm^3 volume. The implication of this scaling is that higher-resolution 3D printing can *geometrically enhance* 3D electronic conduction. For example, structures with 10 μm features at the limits of industrial μSLA would offer 20× higher conductance for a given coating compared with 200 μm printed features as might be created by lower-resolution 3D-printing methods such as FDM. It is interesting to note that the more geometrically complex face-centered-cubic (fcc) lattices printed by SLA have been theoretically predicted to have approximately twice the relative electrical conductivity compared with diamond or simple cubic lattices for a given unit cell size and element resistance.[35]

The electrical geometric advantages of 3D lattices derive from their enhanced surface area compared with planar films. As shown in Figure 4D, conductive 3D lattices can reach surface areas multiple orders of magnitude higher than planar films with the same 2D footprint, providing enhancement of 400× over 2D films in the case of the octet lattices printed in this study. This surface area enhancement scales inversely with the lattice constant for high-resolution, dense 3D lattices. We also note that the surface area of the 3D porous structures has been demonstrated to be essential for determining performance in applications to electrochemical energy storage,[36] electrocatalysis,[37] and 3D-printed fuel cells.[38] Likewise, surface area has previously been proven an important factor for determining sensitivity of metal oxide nanomaterials to various chemical analytes, such as liquids and gases.[39] To build on these theoretical advantages and capture the benefits of 3D mesostructures for electronic sensing, we now combine these optimal geometries with nanoscale design of metal oxide electrostatics, leveraging the precision of ALD.

Three-dimensional device fabrication toward multimodal sensing

The conductive lattices were applied as *multimodal* chemical, thermal, and mechanical sensors to explore the 3D enhancements to their sensing functionality. Although a much larger set of 3D electronic structures could be fabricated by the methods presented in this work, these sensing studies specifically implement octet lattices for sensing due to their favorable 3D geometry, offering high surface area-to-volume ratios[22] in combination with their higher theoretically predicted electrical conductivity and thermal conductivity compared with simple cubic or diamond lattices.[35,40] The 3D lattices composed of ultrathin ZnO were implemented as room-temperature, low-power gas sensors, showing a significant response to volatile organic compounds (VOCs), including ethanol, isopropyl alcohol, and acetone, in the range of 1–10,000 ppm without requiring the high power consumption of embedded heaters used in state-of-the-art commercial gas sensors.[41] We note that the high dynamic range of VOC sensing achieved with our 3D-printed sensors exceeds that demonstrated with gas sensors fabricated through sputtering or spray coating of ZnO, which require substantially higher processing temperatures.[42–44] A fascinating feature of the 3D geometries is the enhancement of the relative change in resistance at a given gas concentration with respect to 2D films deposited by the same ALD process. For example, 3D lattices with ultrathin 11 nm ZnO coatings show a 100× enhancement of sensitivity relative to identical 2D films for ethanol sensing at the

Please cite this article in press as: Huddy et al., Transforming 3D-printed mesostructures into multimodal sensors with nanoscale conductive metal oxides, Cell Reports Physical Science (2022), https://doi.org/10.1016/j.xcrp.2022.100786

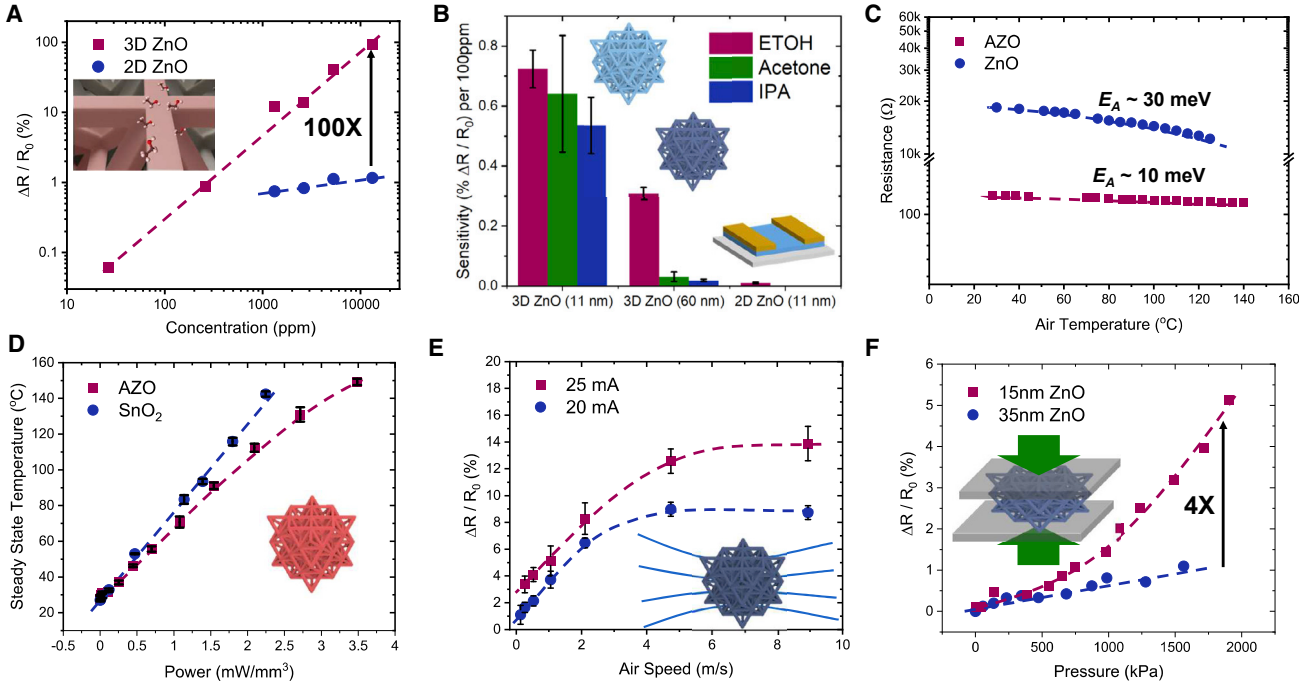

Figure 5. Enhanced sensing capabilities of conductive 3D lattices

(A) Comparison of chemiresistive volatile organic gas (EtOH) sensing with 3D octet and 2D ZnO gas sensors.

(B) Sensitivity comparison between thick and thin 3D ZnO coatings and 2D ZnO films on SiO_2 for detection of ethanol (EtOH), acetone, and isopropanol (IPA). Error bars indicate standard deviation.

(C) Temperature-dependent resistance of 3D AZO conductor and ZnO semiconductor lattices.

(D) Steady-state temperature of AZO- and SnO_2-coated 3D lattices as a function of applied power for joule heating with error bars indicating standard deviation.

(E) The 3D anemometer resistive response to variable air velocity with error bars indicating standard error.

(F) Resistive response of 15 and 35 nm ZnO-coated 3D lattices to compressive mechanical loading at varying pressure, showing an ~4× difference in gauge factor.

parts per million level (Figure 5A). This trend holds for multiple gaseous analytes and across a large dynamic range (1,000×) of gas concentrations, illustrating the power of 3D geometrical design to enhance sensing functionality of metal oxides (Figure 5B). Importantly, unlike various other 2D film-based gas sensors, the 3D geometries shown here achieve high surface area while allowing for operation as *flow-through* sensors requiring no additional bulky packaging. We note that the 3D printing process here also minimizes the necessary footprint of the sensors, eliminating the need for larger arrays of interdigitated electrodes patterned by photolithography[45] used in the state of the art.

This demonstrated ability to grow ultrathin semiconducting and conducting films with controlled thickness at the nanometer scale is extremely important for tuning the electrostatics toward sensing applications. Semiconductor films, including inorganic oxides utilized for liquid and gaseous sensing, have an electrostatic surface sensitivity determined by their thickness relative to the Debye length (L_D),

$$L_D = \sqrt{\frac{\varepsilon k_B T}{q^2 n}}. \qquad \text{(Equation 3)}$$

For example, the VOC sensing capabilities of 3D lattice structures with thin (11 nm) and thick (60 nm) ZnO were compared, as shown in Figure 5B, illustrating the enhanced resistive response of the ZnO 3D structures. Debye length estimates

based on carrier concentration for the more resistive ultrathin 11 nm (L_D ~25 nm) and more conductive 60 nm (L_D ~2 nm) ZnO help to directly explain the enhanced chemiresistive response at low VOC gas concentrations. It is well known that thinner semiconductor films for which $t_s < L_D$ have surface-dominated electrostatic interactions with physisorbed gas molecules.[46] The power of our growth method is the ability of the Al_2O_3 seed layer to facilitate uniform ultrathin growth at the nanometer scale required to achieve room-temperature chemical sensitivity of metal oxides[47] for ultra-low-power Internet of Things (IoT) applications.

Similarly, highly conductive films of AZO and SnO_2 at thicknesses of approximately 100 nm facilitate *multimodal*, thermophysical sensing. Figure 5C illustrates the variation in resistance of 3D ZnO- and AZO-coated octet lattices with temperature, illustrating the enhanced response of semiconducting ZnO functioning as a thermistor. The low thermal mass of these porous 3D lattice structures has considerable advantages for enhancing its response to rapid changes in air temperature. As shown in Figure S10, the 3D structures sense air temperature changes with a first-order time constant of approximately 340 ms, comparable to state-of-the-art fine-gauge thermocouple elements but offering a variety of opportunities for structural 3D integration.

Thicker films of degenerate SnO_2 and AZO with resistance approaching 100 Ω, however, also offer the ability to distribute self-heating throughout the 3D lattice, as shown in Figure 5D. Using infrared thermometry, the lattice structures were observed to rapidly heat to temperatures from 40°C to 140°C with less than 3.0 mW/mm^3 of applied power. As shown in Figure S11, the first-order time constant for internal joule heating of these structures is approximately 200 ms, which is useful for various sensing applications that require higher temperatures to operate effectively.[48] We also demonstrate how the self-heating function of these low-thermal-mass, free-standing 3D structures facilitates their implementation as *thermal anemometer flow sensors* for detecting the convective cooling of the lattice with air flowing through it, as demonstrated in Figure 5E. Self-heated octet structures allow anemometry across an approximately 40× dynamic range of air velocities from 0.13 to 5 m/s. These devices achieve a sensitivity of approximately 1–2 mV/(m/s)/mW in the linear regime (Figure S12), which is comparable to the sensitivity reported for state-of-the-art microelectromechanical systems (MEMS) hot-wire anemometers.[49,50] To put this result in context, we note that our millimeter-scale 3D-printed anemometer can achieve high sensitivity without requiring photolithography and complex etching steps and that it is more compact than commercial products.

Finally, we demonstrate the ability of these ceramic-coated, conductive 3D structures to serve as custom pressure sensors. Figure 5F illustrates resistance changes in response to applied pressure for octet lattices with different thickness of ZnO coatings (15 and 35 nm). Figure S13 shows a linear relationship between strain and force, which can be expressed as an effective modulus (200 MPa) for the 3D lattice structures, dictated by the strut parameters such as radius, height, arrangement, etc.[51,52] The resistance change with increasing pressure shown in the Figure 5F is more pronounced for the lattice with thinner ZnO within a pressure and strain range up to 20 kPa and 1.2% uniaxial strain (Figure S13). The 4× improved sensitivity in the thinner coating is reflected commensurately in the gauge factor (GF), which reached approximately 6.2 ± 1.2 and 1.4 ± 0.7 for 15 and 35 nm thick films, respectively, at a value of 1.3% compressive strain (Figure S14). This exceeds the GF of 2 reported for recent state-of-the-art 3D-printed load cells incorporating carbon nanotube (CNT)-based composites.[53] We note that these GFs match well with the piezoresistive properties of ZnO reported in the literature for planar strain

Please cite this article in press as: Huddy et al., Transforming 3D-printed mesostructures into multimodal sensors with nanoscale conductive metal oxides, Cell Reports Physical Science (2022), https://doi.org/10.1016/j.xcrp.2022.100786

sensors.[54–56] The increment in GF can be attributed to the thinner coating being more semiconducting and less metallic compared with the thicker ZnO, in accordance with previous work.[54] This demonstrates the unique tunability in mechanical response that stems directly from the ability of this strategy to coat nanoscale semiconductor films. In addition, we note that it is possible to modify the effective modulus of the 3D-printed polymer structures by simply changing the lattice geometry (e.g., beam thickness), which will allow tuning of the force sensing range without modifying the sensing material.[52] The 3D ALD coating provides a basis for the future design of custom mechanical sensing elements in various custom geometries for microrobotics requiring sensitivity to a high dynamic range of forces.

In summary, we present a unique strategy for fabricating multifunctional 3D electronic devices by transforming 3D-printed polymers through the deposition of nanoscale conductive metal oxides. This process combines multimaterial ALD growth of conductive, insulating, and semiconducting films with high-resolution μSLA to produce 3D lattices with microscale features down to 10 μm that demonstrate geometric advantages for electronic transport. We also apply a graph-theory-based approach to model 3D conductive networks and explore the potential for 3D scaling to enhance both conductance and multimodal sensing by engineering high-surface-area mesostructures. The unique capabilities of our strategy for 3D electronic integration bridge nanoscale electronic material design to micro- and mesoscale device design, allowing a unique multifunctionality applicable to fluid, thermal, chemical, and mechanical sensing. By tuning the nanoscale conductive coatings, we engineered mesoscale structures with 100× improved sensitivity compared with 2D counterpart devices for room-temperature, low-power gas sensing. This is possible through precision control of the ultrathin metal oxide thin films' electrostatically driven surface sensitivity. In combination with the design freedom offered by 3D printing, we anticipate that this innovation will unlock a tremendous variety of applications in mesoscale devices, from implanted biomedical sensors to rapid custom fabrication of 3D integrated microelectromechanical systems.

EXPERIMENTAL PROCEDURES

Resource availability

Lead contact

Further information requests should be directed to and will be fulfilled by the lead contact, William Scheideler (william.j.scheideler@dartmouth.edu).

Materials availability

This study did not generate new unique reagents.

Data and code availability

All data are available in the main text or the supplementary materials. All source codes are available upon request.

Microscale 3D printing and atomic layer deposition

The 3D lattice structures were produced by μSLA using a microArch S240 3D printer from Boston Microfabrication (BMF) with pixel size ranging from 2 to 10 μm and layer thickness of 10 μm. The 3D structures were fabricated using a highly rigid and thermally stable polyurethane acrylate resin ("HTL") developed by BMF with a T_g of 172°C, a tensile strength of 79.3 MPa, and resin viscosity of 85 cP. ALD film growth was performed on an Anric AT-400 system at temperatures from 100°C to 175°C using TMA, diethylzinc (DEZ), and tetrakis(dimethylamino)tin(IV) (TDMA-Sn). Growth of films from 5 to 100 nm was done using 40 sccm N_2 flow and a nominal chamber pressure of 130 mT, completing a varied number of cycles. One complete ALD cycle consisted of three

pulses of DEZ/TMA/TDMA-Sn and two oxidant pulses (H_2O for TMA/DEZ and O_3 for TDMA-Sn). To produce AZO, we doped ZnO films with 5 at % Al_2O_3 by using a ratio of 19:1 cycles of ZnO:Al_2O_3. The TDMA-Sn precursor was heated to 70°C to increase its vapor pressure. All 3D-printed microlattices used in this paper were developed using the BMF HTL resin in yellow. In addition to this resin, we have shown that the seed layer process described in the main text also works for parts made with the BMF HTL resin in black, CADworks 3D MiiCraft BV-007A Microfluidics resin, Kudo 3D UHR resin, Formlabs Rough 4000 resin, Formlabs Tough 2000 resin, and Formlabs High Temp resin.

Three-dimensional device fabrication

Conformal Au electrodes (20 nm thick) for measurements of the 3D structures were deposited by sputtering (Hummer) and physically masking the channel area with a thin polyimide (Kapton) tape with acrylic adhesive. The tape was removed to reveal masked 3D channels through the lattice structures with critical dimensions from 1 to 4 mm in length. DC electrical measurements (B2902A) were performed on a semiconductor probe station using micropositioners with tungsten needle probes to contact the 3D structures (Figure S6). The use of the Au metal contacts ensured measurement variability of less than 2% (Figure S6). Batch-to-batch variability of resistance across multiple 3D lattices was measured to be approximately $\pm$10%. The study of 3D lattice resistance for variable SnO_2 coating thicknesses (Figure 3C) was performed through ALD growth of incrementally thicker layers. The seed layer was deposited, followed by the first increment of SnO_2, after which sputtered gold electrodes were deposited to facilitate precise measurements. Thicker SnO_2 films were coated onto this structure for subsequent measurements.

Microscopy and material characterization

SEM/EDS analysis was performed with a Thermo Fisher Scientific Helios 5 CX DualBeam SEM. XRD studies were performed on the coated 3D and 2D structures using a Rigaku Ultrax-18 system with a Cu Kα line source with a step size of 0.01°. XPS analysis was performed with a Kratos Axis Supra.

Graph theory calculation of 3D structure conductivity

The estimated resistance of the cubic volumes of octet lattice plotted in Figures 3C and 3D were computed in MATLAB by using a weighted Laplacian representation of the octet lattice, as described in the main text. The graph object is generated based on the exact geometry of the octet truss system. Each beam is represented with an edge in the graph, which has a corresponding weight (conductance) given by its resistance, as calculated by Equation (1) using the measured sheet resistance data. Calculation of the pseudo-inverse of the weighted Laplacian allows efficient computation of the effective resistance between any two points. To match the experimental conditions for the cubic structures with sputtered electrodes, the simulation adjusts the conductance weights for the faces coated in Au to match the predicted conductivity for a 20 nm sputtered Au coating. Simulations were conducted for cubic volumes as well as higher aspect ratio structures as shown in Figure 3D to extract a resistance per cube.

Sensor characterization

Gas sensing measurements were conducted using dry air for purging a closed chamber. VOCs were dosed as liquids (ethanol, isopropanol, or acetone) onto a Peltier heating element, while the resistances of the cube and a 2D film on SiO_2 were simultaneously measured with a B2902A source meter. The self-heating experiment was conducted by driving a current across the cube and measuring the cube temperature

with a FLIR E60 IR camera. Anemometers were characterized in a flow-through mode, using $^{3}/_{8}''$ tubing. Cube response to different air temperatures was measured by monitoring the resistance change across the cube as the temperature of the cube was changed with the cube resting in an oven during measurement. Air temperature response of cubes was measured with the cube sitting at the outlet of a $^{3}/_{8}''$ tube with a flow rate of 20 lpm. The sensor lattices were attached to 28G Cu wire and suspended in the tubing throughout the measurement. A flow meter was used to set a known airflow rate through the channel. The pressure sensors were tested under compression mode with a mechanical testing system (Pasco ME-8236) while logging the resistance measured in the direction of compressive loading (Figure S15).

SUPPLEMENTAL INFORMATION

Supplemental information can be found online at https://doi.org/10.1016/j.xcrp.2022.100786.

ACKNOWLEDGMENTS

We acknowledge support from Boston Microfabrication. We also acknowledge John Wilderman at the University of New Hampshire for his help in completing XPS measurements. Support for the NH BioMade Project is provided by the National Science Foundation through EPSCoR Research Infrastructure Improvement Award 1757371. Funding for this work was provided by National Science Foundation grant AWD00011316. A.B.H. was supported by a National Science Foundation Graduate Research Fellowship.

AUTHOR CONTRIBUTIONS

Conceptualization, W.J.S. and J.E.H.; methodology, W.J.S., J.E.H., and M.S.R.; device design and fabrication, J.E.H.; modeling, W.J.S.; materials characterization, J.E.H., Y.Y., and A.B.H.; device characterization, J.E.H., M.S.R., and W.J.S.; formal analysis, J.E.H., M.S.R., A.B.H., Y.Y., and W.J.S.; writing—original draft, W.J.S.; writing—review & editing, W.J.S., J.E.H., M.S.R., A.B.H., and Y.Y.; visualization, W.J.S., J.E.H., and M.S.R.; supervision, W.J.S.

DECLARATION OF INTERESTS

The authors declare no competing interests.

Received: September 23, 2021
Revised: February 1, 2022
Accepted: February 3, 2022
Published: February 25, 2022

REFERENCES

1. Meza, L.R., Das, S., and Greer, J.R. (2014). Strong, lightweight, and recoverable three-dimensional ceramic nanolattices. Science *345*, 1322–1326.

2. Wendy Gu, X., and Greer, J.R. (2015). Ultra-strong architected Cu meso-lattices. Extreme Mech. Lett. *2*, 7–14.

3. Murphy, S.V., and Atala, A. (2014). 3D bioprinting of tissues and organs. Nat. Biotechnol. *32*, 773–785.

4. Zhang, L., Yang, G., Johnson, B.N., and Jia, X. (2019). Three-dimensional (3D) printed scaffold and material selection for bone repair. Acta Biomater. *84*, 16–33.

5. Ntouanoglou, K., Stavropoulos, P., and Mourtzis, D. (2018). 4D printing prospects for the aerospace industry: a critical review. Proced. Manufacturing *18*, 120–129.

6. Hu, Y., Guo, Z., Ragonese, A., Zhu, T., Khuje, S., Li, C., Grossman, J.C., Zhou, C., Nouh, M., and Ren, S. (2020). A 3D-printed molecular ferroelectric metamaterial. Proc. Natl. Acad. Sci. U S A *117*, 27204–27210.

7. Jackson, J.A., Messner, M.C., Dudukovic, N.A., Smith, W.L., Bekker, L., Moran, B., Golobic, A.M., Pascall, A.J., Duoss, E.B., Loh, K.J., et al. (2018). Field responsive mechanical metamaterials. Sci. Adv. *4*, eaau6419.

8. Zhang, G., Zhang, X., Liu, H., Li, J., Chen, Y., and Duan, H. (2021). 3D-Printed multi-channel metal lattices enabling localized electric-field redistribution for dendrite-free aqueous Zn ion batteries. Adv. Energy Mater. *11*, 2003927.

9. Boley, J.W., Rees, W.M.V., Lissandrello, C., Horenstein, M.N., Truby, R.L., Kotikian, A., Lewis, J.A., and Mahadevan, L. (2019). Shape-shifting structured lattices via multimaterial 4D printing. Proc. Natl. Acad. Sci. U S A *116*, 20856–20862.

10. Beck, V.A., Ivanovskaya, A.N., Chandrasekaran, S., Forien, J.-B., Baker, S.E., Duoss, E.B., and Worsley, M.A. (2021). Inertially enhanced mass transport using 3D-printed porous flow-through electrodes with periodic lattice structures. Proc. Natl. Acad. Sci. U S A *118*, e2025562118.

11. Ge, Q., Li, Z., Wang, Z., Kowsari, K., Zhang, W., He, X., Zhou, J., and Fang, N.X. (2020). Projection micro stereolithography based 3D printing and its applications. Int. J. Extrem. Manuf. *2*, 022004.

12. Hahn, V., Kiefer, P., Frenzel, T., Qu, J., Blasco, E., Barner-Kowollik, C., and Wegener, M. (2020). Rapid assembly of small materials building blocks (voxels) into large functional 3D metamaterials. Adv. Funct. Mater. *30*, 1907795.

13. Manapat, J.Z., Chen, Q., Ye, P., and Advincula, R.C. (2017). 3D printing of polymer nanocomposites via stereolithography. Macromolecular Mater. Eng. *302*, 1600553.

14. Eckel, Z.C., Zhou, C., Martin, J.H., Jacobsen, A.J., Carter, W.B., and Schaedler, T.A. (2016). Additive manufacturing of polymer-derived ceramics. Science *351*, 58–62.

15. Su, X., Li, X., Ong, C.Y.A., Herng, T.S., Wang, Y., Peng, E., and Ding, J. (2019). Metallization of 3D printed polymers and their application as a fully functional water-splitting system. Adv. Sci. *6*, 1801670.

16. Egorov, V., Gulzar, U., Zhang, Y., Breen, S., and O'Dwyer, C. (2020). Evolution of 3D printing methods and materials for electrochemical energy storage. Adv. Mater. *32*, 2000556.

17. Song, J., Chen, Y., Cao, K., Lu, Y., Xin, J.H., and Tao, X. (2018). Fully controllable design and fabrication of three-dimensional lattice supercapacitors. ACS Appl. Mater. Inter. *10*, 39839–39850.

18. Song, B., Kenel, C., and Dunand, D.C. (2020). 3D ink-extrusion printing and sintering of Ti, Ti-TiB and Ti-TiC microlattices. Additive Manufacturing *35*, 101412.

19. Saleh, M.S., Hu, C., Brenneman, J., Al Mutairi, A.M., and Panat, R. (2021). 3D printed three-dimensional metallic microlattices with controlled and tunable mechanical properties. Additive Manufacturing *39*, 101856.

20. Shimizu, Y., and Egashira, M. (1999). Basic aspects and challenges of semiconductor gas sensors. MRS Bull. *24*, 18–24.

21. Nakatsuka, N., Yang, K.-A., Abendroth, J.M., Cheung, K.M., Xu, X., Yang, H., Zhao, C., Zhu, B., Rim, Y.S., Yang, Y., et al. (2018). Aptamer–field-effect transistors overcome Debye length limitations for small-molecule sensing. Science *362*, 319–324.

22. Egan, P.F., Gonella, V.C., Engensperger, M., Ferguson, S.J., and Shea, K. (2017). Computationally designed lattices with tuned properties for tissue engineering using 3D printing. PLoS One *12*, e0182902.

23. Zheng, X., Lee, H., Weisgraber, T.H., Shusteff, M., DeOtte, J., Duoss, E.B., Kuntz, J.D., Biener, M.M., Ge, Q., Jackson, J.A., et al. (2014). Ultralight, ultrastiff mechanical metamaterials. Science *344*, 1373–1377.

24. Buj-Corral, I., Domínguez-Fernández, A., and Durán-Llucià, R. (2019). Influence of print orientation on surface roughness in fused deposition modeling (FDM) processes. Materials *12*, 3834.

25. Zhao, H., Ye, C., Xiong, S., Fan, Z., and Zhao, L. (2020). Fabricating an effective calcium zirconate layer over the calcia grains via binder-jet 3D-printing for improving the properties of calcia ceramic cores. Additive Manufacturing *32*, 101025.

26. Cho, T.H., Farjam, N., Allemang, C.R., Pannier, C.P., Kazyak, E., Huber, C., Rose, M., Trejo, O., Peterson, R.L., Barton, K., et al. (2020). Area-selective atomic layer deposition patterned by electrohydrodynamic jet printing for additive manufacturing of functional materials and devices. ACS Nano *14*, 17262–17272.

27. Chawla, V., Ruoho, M., Weber, M., Chaaya, A.A., Taylor, A.A., Charmette, C., Miele, P., Bechelany, M., Michler, J., and Utke, I. (2019). Fracture mechanics and oxygen gas barrier properties of Al2O3/ZnO nanolaminates on PET deposited by atomic layer deposition. Nanomaterials *9*, 88.

28. Yang, F., Brede, J., Ablat, H., Abadia, M., Zhang, L., Rogero, C., Elliott, S.D., and Knez, M. (2017). Reversible and irreversible reactions of Trimethylaluminum with common organic functional groups as a model for molecular layer deposition and vapor phase infiltration. Adv. Mater. Inter. *4*, 1700237.

29. Parsons, G.N., Atanasov, S.E., Dandley, E.C., Devine, C.K., Gong, B., Jur, J.S., Lee, K., Oldham, C.J., Peng, Q., Spagnola, J.C., et al. (2013). Mechanisms and reactions during atomic layer deposition on polymers. Coord. Chem. Rev. *257*, 3323–3331.

30. Kavan, L., Steier, L., and Grätzel, M. (2017). Ultrathin buffer layers of SnO2 by atomic layer deposition: perfect blocking function and thermal stability. J. Phys. Chem. C *121*, 342–350.

31. Lim, S.J., Kwon, S., and Kim, H. (2008). ZnO thin films prepared by atomic layer deposition and rf sputtering as an active layer for thin film transistor. Thin Solid Films *516*, 1523–1528.

32. Beh, H., Hiller, D., and Zacharias, M. (2018). Optimization of ALD-ZnO thin films toward higher conductivity. Physica Status Solidi (a) *215*, 1700880.

33. Farva, U., and Kim, J. (2021). Growth temperature-dependent morphological, optical, and electrical study of SnO2 thin film by atomic layer deposition. Mater. Chem. Phys. *267*, 124584.

34. Van Mieghem, P., Devriendt, K., and Cetinay, H. (2017). Pseudoinverse of the Laplacian and best spreader node in a network. Phys. Rev. E *96*, 032311.

35. Melnikov, A.V., Shuba, M., and Lambin, P. (2018). Modeling the electrical properties of three-dimensional printed meshes with the theory of resistor lattices. Phys. Rev. E *97*, 043307.

36. Liu, Z., Yuan, X., Zhang, S., Wang, J., Huang, Q., Yu, N., Zhu, Y., Fu, L., Wang, F., Chen, Y., et al. (2019). Three-dimensional ordered porous electrode materials for electrochemical energy storage. NPG Asia Mater. *11*, 1–21.

37. Lee, C.-Y., Taylor, A.C., Nattestad, A., Beirne, S., and Wallace, G.G. (2019). 3D printing for electrocatalytic applications. Joule *3*, 1835–1849.

38. Calignano, F., Tommasi, T., Manfredi, D., and Chiolerio, A. (2015). Additive manufacturing of a microbial fuel cell—a detailed study. Scientific Rep. *5*, 17373.

39. Wang, B., Zhu, L.F., Yang, Y.H., Xu, N.S., and Yang, G.W. (2008). Fabrication of a SnO2 nanowire gas sensor and sensor performance for hydrogen. J. Phys. Chem. C *112*, 6643–6647.

40. Wang, N., Kaur, I., Singh, P., and Li, L. (2021). Prediction of effective thermal conductivity of porous lattice structures and validation with additively manufactured metal foams. Appl. Therm. Eng. *187*, 116558.

41. Gomes, J.B.A., Rodrigues, J.J.P.C., Rabêlo, R.A.L., Kumar, N., and Kozlov, S. (2019). IoT-enabled gas sensors: technologies, applications, and opportunities. J. Sensor Actuator Networks *8*, 57.

42. Al-Hardan, N.H., Abdullah, M.J., Abdul Aziz, A., Ahmad, H., and Low, L.Y. (2010). ZnO thin films for VOC sensing applications. Vacuum *85*, 101–106.

43. Teimoori, F., Khojier, K., and Dehnavi, N.Z. (2017). Investigation of sensitivity and selectivity of ZnO thin film to volatile organic compounds. J. Theor. Appl. Phys. *11*, 157–163.

44. Kulandaisamy, A.J., Elavalagan, V., Shankar, P., Mani, G.K., Babu, K.J., and Rayappan, J.B.B. (2016). Nanostructured Cerium-doped ZnO thin film – a breath sensor. Ceramics Int. *42*, 18289–18295.

45. Acuautla, M., Bernardini, S., Gallais, L., Fiorido, T., Patout, L., and Bendahan, M. (2014). Ozone flexible sensors fabricated by photolithography and laser ablation processes based on ZnO nanoparticles. Sensors Actuators B: Chem. *203*, 602–611.

46. Bai, J., Zhao, C., Gong, H., Wang, Q., Huang, B., Sun, G., Wang, Y., Zhou, J., Xie, E., and Wang, F. (2019). Debye-length controlled gas sensing performances in NiO@ZnO p-n junctional core–shell nanotubes. J. Phys. D: Appl. Phys. *52*, 285103.

47. Shankar, P., and Rayappan, J.B.B. (2017). Monomer: design of ZnO nanostructures (nanobush and nanowire) and their room-temperature ethanol vapor sensing signatures. ACS Appl. Mater. Inter. *9*, 38135–38145.

48. Kim, J.-Y., Lee, J.-H., Kim, J.-H., Mirzaei, A., Woo Kim, H., and Kim, S.S. (2019). Realization of H2S sensing by Pd-functionalized networked CuO nanowires in self-heating mode. Sensors Actuators B: Chem. *299*, 126965.

49. Mailly, F., Giani, A., Bonnot, R., Temple-Boyer, P., Pascal-Delannoy, F., Foucaran, A., and Boyer, A. (2001). Anemometer with hot platinum thin film. Sensors Actuators A: Phys. *94*, 32–38.

50. Talbi, A., Gimeno, L., Gerbedoen, J.-C., Viard, R., Soltani, A., Mortet, V., Preobrazhensky, V.,

Merlen, A., and Pernod, P. (2015). A micro-scale hot wire anemometer based on low stress (Ni/W) multi-layers deposited on nano-crystalline diamond for air flow sensing. J. Micromech. Microeng. *25*, 125029.

51. Arretche, I., and Matlack, K.H. (2018). On the interrelationship between static and vibration mitigation properties of architected metastructures. Front. Mater. https://doi.org/10.3389/fmats.2018.00068.

52. Bagheri, A., Buj-Corral, I., Ferrer Ballester, M., Magdalena Pastor, M., and Roure Fernandez, F. (2018). Determination of the elasticity modulus of 3D-printed octet-truss structures for use in porous prosthesis implants. Materials *11*, 2420.

53. Joung, K.-Y., Kim, S.-Y., Kang, I., and Cho, S.-H. (2021). 3D-Printed load cell using nanocarbon composite strain sensor. Sensors *21*, 3675.

54. Inomata, N., Toan, N.V., and Ono, T. (2017). Piezoresistive property of an aluminum-doped zinc oxide thin film deposited via atomic-layer deposition for microelectromechanical system/nanoelectromenchanical system applications. IEEJ Trans. Electr. Electron. Eng. *12*, S120–S124.

55. Cardoso, G.W.A., Leal, G., da Silva Sobrinho, A.S., Fraga, M.A., and Massi, M. (2014). Evaluation of piezoresistivity properties of sputtered ZnO thin films. Mat. Res. *17*, 588–592.

56. Tuyaerts, R., Poncelet, O., Raskin, J.-P., and Proost, J. (2017). Internal stress and opto-electronic properties of ZnO thin films deposited by reactive sputtering in various oxygen partial pressures. J. Appl. Phys. *122*, 155306.